

Relevance of mask-roughness-induced printed line-edge roughness in recent and future extreme-ultraviolet lithography tests

Patrick P. Naulleau

The control of line-edge roughness (LER) of features printed in photoresist poses significant challenges to next-generation lithography techniques such as extreme-ultraviolet (EUV) lithography. Achieving adequately low LER levels requires accurate resist characterization as well as the ability to separate resist effects from other potential contributors to LER. One potentially significant contributor to LER arises from roughness on the mask coupling to speckle in the aerial image and consequently to LER in the printed image. Here I numerically study mask surface roughness and phase roughness to resist LER coupling both as a function of illumination coherence and defocus. Moreover, the potential consequences of this mask effect for recent EUV lithography experiments is studied through direct comparison with experimental through-focus printing data collected at a variety of coherence settings. Finally, the effect that mask roughness will play in upcoming 0.3-numerical-aperture resist testing is considered.

© 2004 Optical Society of America

OCIS codes: 110.3960, 110.4980, 030.5770, 030.6140, 260.7200.

1. Introduction

Line-edge roughness (LER), has become of increasing concern as projection lithography techniques push to smaller and smaller feature sizes. This poses significant challenges to the development of photoresist for next-generation lithography techniques such as extreme-ultraviolet (EUV) lithography.¹⁻³ For example, at the 45-nm fabrication node, the International Technology Roadmap for Semiconductors⁴ calls for a resist contribution to LER of less than 2 nm, which in turn requires even finer characterization capabilities for developing such resists.

The accuracy of resist LER characterization accuracy depends on several factors beyond simple metrology constraints, including the difficult problem of separating resist contributions to the experimentally measured LER from other contributors. Much effort has been directed toward characterizing EUV resists,⁵⁻⁸ with the most straightforward being projection lithography tests with advanced EUV lithography tools.⁸⁻¹⁰ Use of these tools for LER

characterization, however, requires a careful analysis of all tool-level contributions to LER. One such system-level effect, LER on the mask coupling to printed LER, has already been studied,¹¹ showing that current mask technology must be significantly improved in order to meet the 45-nm node requirement,⁴ let alone that of subsequent nodes.

Another potentially important contribution from the mask, however, is surface roughness coupling to speckle in the aerial image and consequently to LER in the printed pattern.^{12,13} EUV lithography, which is based on reflective optics and masks, is particularly vulnerable to this problem because mask roughness is geometrically coupled to phase roughness, scaled by an additional factor of 2 owing to reflection. Utilizing a wavelength of nominally 13.4 nm means that very small levels of roughness on the multi-layer-coated mask can contribute to significant modulation of the phase. Although the lithographic process involves reimaging the mask to the wafer, the process remains sensitive to phase errors at the mask by virtue of the band-limited imaging process. Moreover, as defocus is introduced into the system, the imaging condition no longer strictly holds, and phase errors at the mask directly couple to intensity variation or speckle. The problem becomes increasingly severe as the illumination coherence is increased,¹⁴ as is often the case when using resolution-enhancing pupil fills.

Here I numerically study mask surface roughness

The author (pnaulleau@lbl.gov) is with the Center for X-Ray Optics, Lawrence Berkeley National Laboratory, 1 Cyclotron Road, Berkeley, California 94720.

Received 2 February 2004; revised manuscript received 4 April 2004; accepted 26 April 2004.

0003-6935/04/204025-08\$15.00/0

© 2004 Optical Society of America

and phase roughness to resist LER coupling both as a function of illumination coherence and defocus. Moreover, the potential consequences of this mask effect for recent EUV lithography experiments is studied through direct comparison with experimental through-focus printing data collected at a variety of coherence settings. Finally, the effect that mask roughness will play in upcoming 0.3-numerical-aperture resist testing is considered.

2. Analysis Approach

In principle, the problem of mask surface roughness coupling to line-edge roughness can be addressed analytically by use of partially coherent image formation theory combined with the statistical representation of the mask as a random-phase object¹³; however, the problem quickly becomes intractable even under the small-phase perturbation approximation. Moreover, an analytic solution becomes even more complex as defocus is considered or as the small-phase perturbation approximation breaks down.

An alternative analytical approach could be to use geometric optics while describing the rough mask in terms of slope error. Although this simple approach provides a convenient mechanism for visualizing defocus effects, it completely fails to account for the effect of partial coherence on the physical process. Given that the mask-roughness-induced LER is fundamentally a speckle issue,¹⁴ coherence plays a crucial role. Moreover, the extent to which speckle (small spatial-scale intensity variation) couples to LER depends on the aerial-image line-edge slope. Given a fixed speckle contrast, the LER would be worse with a smaller line-edge slope. This factor is also ignored by the geometric analysis.

Given the difficulties with the analytic approaches described above, numeric modeling of the partially coherent imaging process remains the most viable method for studying relevant cases of mask-roughness-induced LER. This approach has previously been used to study the in-focus dependence of LER on mask roughness and illumination partial coherence.¹² The numeric modeling approach, however, can readily be extended to study arbitrary imaging conditions, including defocus, as well as any other wave-front aberration.

The modeling used here relies on a numeric implementation of partially coherent image formation equations,¹⁴ coupled with a random-phase-object description of the mask. Defocus as well as other aberrations can be accounted for by modifying the pupil function of the modeled imaging system. Commercial examples of programs providing the required partially coherent image modeling capability include PROLITH¹⁵ and SOLID-C.¹⁶

Of significant concern for analyzing meaningful situations of mask-roughness-induced LER is the description of the roughness in the model. Masks used in EUV lithography are reflective and are rendered so through the deposition of a multilayer coating composed typically of 40 or more bilayers.¹⁷ If one starts

with knowledge of the uncoated substrate surface, multilayer growth models can be used^{18,19} to predict the coating properties throughout the stack. From the calculated coating properties, one can use rigorous electromagnetic field modeling to calculate the electric field reflected from the mask.²⁰⁻²² Such an approach, however, would be extremely time consuming. In most of the cases relevant to the moderate roughness of interest here, the effect of the rough mask can readily be modeled as a pure phase distribution, where the phase is determined from the geometric path-length differences imparted by the assumption that the EUV light is reflected from the top surface of the mask.²³ In practice, this simplification works because the vast majority of the nonconformal multilayer growth occurs within a small number of layers that are closest to the substrate. Within the typical EUV penetration region of approximately 25 bilayers, the multilayer growth tends to be conformal for the roughnesses of interest here. Using this simplified approach, one needs only to measure the topographic profile of the final multi-layer-coated mask.

3. Numeric Study of Mask-Roughness-Induced Line-Edge Roughness

To consider the importance of mask surface roughness on LER-characterization tests, I perform a numeric study by using the modeling methods described above in combination with the simplified representation of the mask roughness. The parameters I choose are selected to coincide with recent EUV print tests performed with a $4\times$ reduction optical system with a numerical aperture (NA) of 0.1.¹⁰ The roughness of the mask used in those tests was measured after final patterning by use of atomic-force microscopy (AFM; see Fig. 1). I note that the measured 0.54-nm rms roughness of that mask is approximately a factor of 2 worse than that of typical high-quality masks available today. To generate the input mask used in the simulations presented here, I calculated the mask surface power-spectral density (PSD; see Fig. 2) from the AFMs and used it to generate a statistical surface of the proper size. Assuming a wavelength of 13.4 nm, I converted the topographic surface to a phase perturbation. This phase distribution was then overlain (multiplied) by an ideal binary amplitude line-space pattern. Figure 3 shows the resulting $4\times$ input mask for features designed to print as 100-nm lines and spaces. The completely black areas represent the absorber regions, and the gray-scale regions represent the wrapped phase of the clear regions on the mask. Although the mask rms surface roughness is only 0.54 nm, upon reflection the induced peak-to-valley phase modulation is greater than 1 wave (2π), based on an illumination wavelength of 13.4 nm.

Figure 4 shows the simulation results for three different printed line widths as a function of focus and the coherence factor, σ . An ideal 0.1-NA EUV optical system has been assumed. The small NA utilized by EUV systems allows the aerial-image modeling to be performed under the thin-mask and

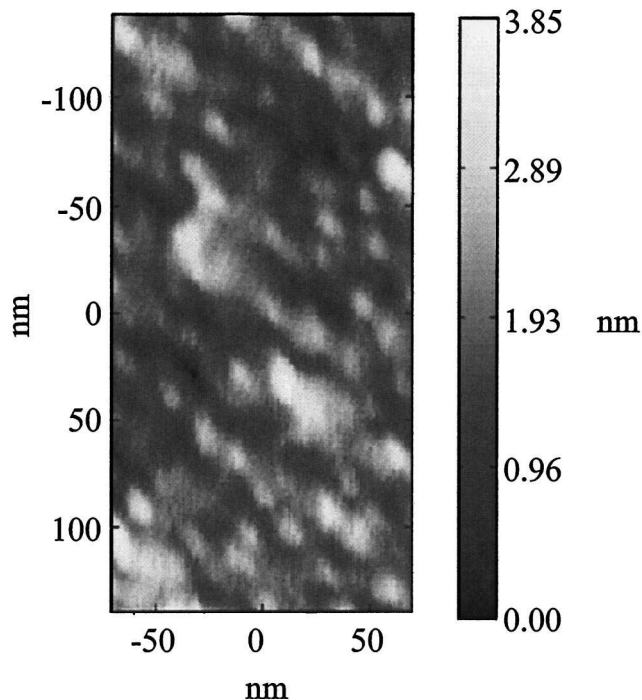


Fig. 1. Atomic force microscope image from a clear area on an EUV mask fabricated for printing with a 0.1-numerical-aperture optic. The rms roughness is 0.54 nm.

scalar models. An ideal binary resist model is used, and the threshold is set separately for each σ value to provide proper sizing of the 100-nm lines at best focus. The single-sided 3σ LER is then calculated from the resulting binary image as the deviation of the measured line edge from a straight line. Interpolation of the line edge is used, allowing the actual threshold position to be determined to a subpixel resolution. For the results presented in this section, an image-space pixel spacing of 1.57 nm was used. In practice, this interpolation is crucial because it allows the aerial-image simulations to be performed over a grid size amenable to current memory and processing limitations. In general we

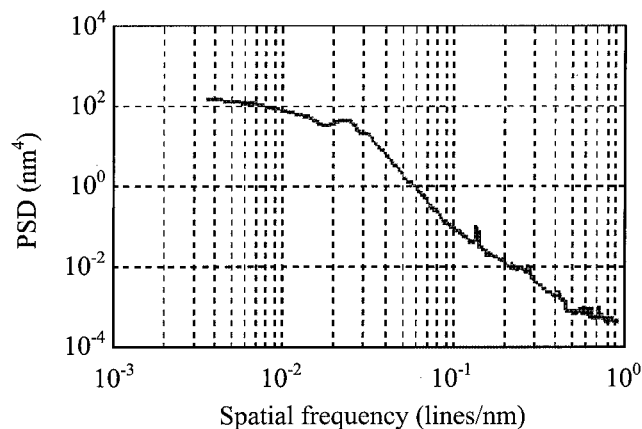


Fig. 2. Isotropic power-spectral density (PSD) based on the AFM in Fig. 1.

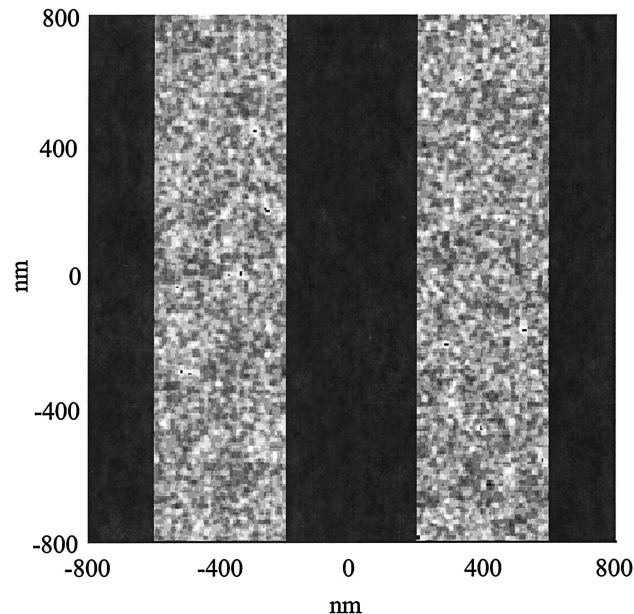


Fig. 3. Representative input $4\times$ mask for aerial-image simulations. Phase roughness is generated based on the PSD in Fig. 2. This particular mask is designed to model 100-nm printed line-space patterns. The solid black regions represent the chrome absorber, and the gray-scale regions represent the wrapped phase, where black is 0 and white is 2π .

see the LER gets worse at smaller line widths, presumably owing to the decreased aerial-image line-edge slope. We also see that defocus plays a crucial role in the mask roughness to LER coupling, with increased coherence enhancing the effect. The increased coherence effect appears to saturate at approximately $\sigma = 0.4$, with LER trends even reversing in some cases. It is interesting to note that at best focus we see very little dependence of LER on the coherence factor and actually consistently observe the LER to increase with σ (decreasing coherence).

Because the modeling process is based on a statistical realization of the mask over a relatively small area (square region 2-cycles wide), it is important to consider statistical variations in the results. This is accomplished by repeating the modeling for a total of 10 independent realizations of the mask roughness. Figure 5 shows LER plots as a function of realization number for the 100-nm case. Each plot represents a single focus value: (a) $-0.8\ \mu\text{m}$, (b) $-0.4\ \mu\text{m}$, and (c) $0\ \mu\text{m}$, with the individual traces representing different partial-coherence values. The plots show a significant LER variation with mask realization; however, the trends seen in Fig. 4 are validated, including reduced LER with increasing coherence at best focus. These results also indicate that the coherence effect saturates at approximately $\sigma = 0.4$ and suggest that the trend reversals with respect to coherence seen in Fig. 4 are not systematic but rather a manifestation of statistical uncertainty.

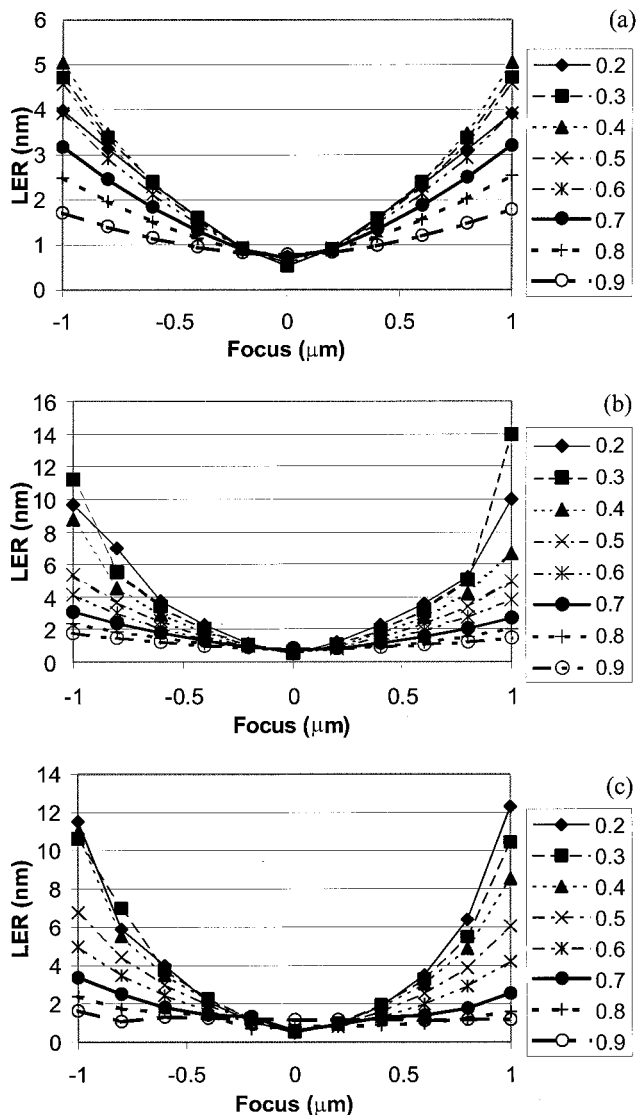


Fig. 4. Simulation results for three different printed line widths as a function of focus and the coherence factor, σ . (a) 100-nm lines and spaces, (b) 90-nm lines and spaces, and (c) 80-nm lines and spaces. An ideal 0.1-NA EUV optical system has been assumed. A binary resist model is used with the threshold set separately for each σ value to provide proper sizing of the 100-nm lines at best focus. The single-sided 3σ LER is then calculated from the resulting binary image.

Improved LER performance at best focus with increasing coherence can be explained heuristically by noting that, in general, the ideal-image line-edge slope also increases with coherence, making it less susceptible to speckle-induced intensity variations. For the LER to be reduced, however, this increased line-edge slope cannot be offset by increasing speckle contrast. In the phenomenon of interest here, image-plane speckle arises from a failure of the optical imaging system to faithfully reproduce the object field. Thus, if one had an ideal infinite-aperture optic, a random-phase object would not produce any intensity variations in the image plane even under coherent illumination. From this point of view, it is

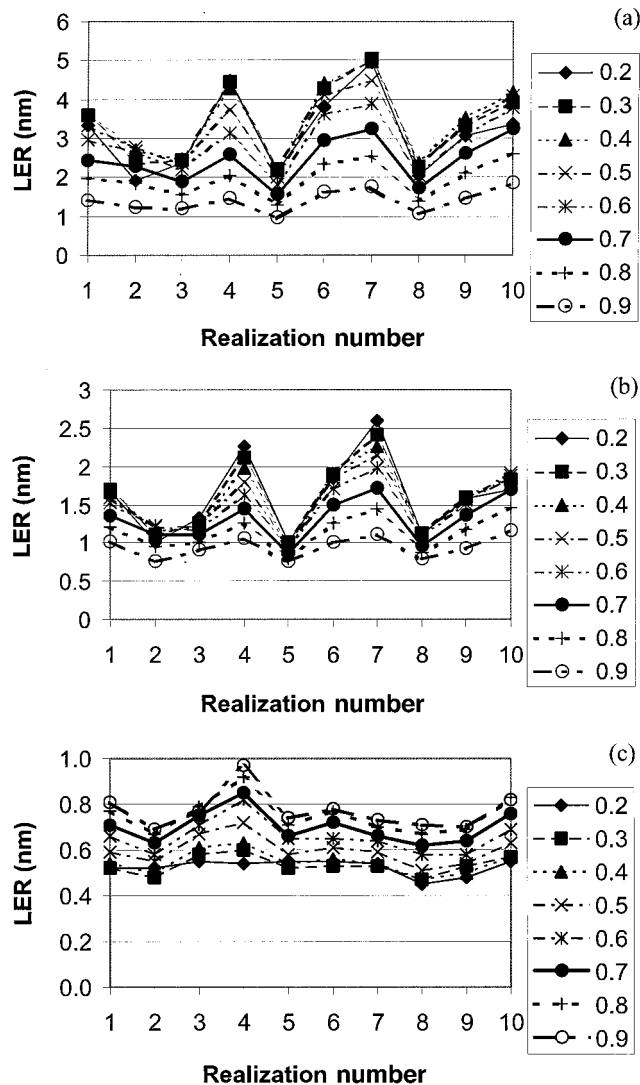


Fig. 5. LER plots as a function of realization number for 10 independent realizations of the rough mask with 100-nm lines and spaces. Each plot represents a single focus value: (a) $-0.8 \mu\text{m}$, (b) $-0.4 \mu\text{m}$, and (c) $0 \mu\text{m}$, with the individual traces representing different partial-coherence values.

evident that the relation between the mask PSD and the optic NA plays a crucial role in determining the in-focus through- σ LER dependence.

Given the strong influence of defocus and the fact that defocus can be thought of simply as an aberration, it is also interesting to consider the role lens aberrations may play in the process. To this end, I repeated the analysis from Fig. 4, incorporating the measured wave-front error²⁴ from the 0.1-NA EUV engineering test stand (ETS) Set-2 optic.²⁵⁻²⁷ The rms wave-front error in the first 37 Zernikes is 0.69 nm. Moreover the wave front used in the modeling incorporates measured frequencies covering a radius of $1.5 \mu\text{m}$ in the image plane. I note that at approximately $\lambda/20$, the wave-front error of the Set-2 optic is approximately two times larger than will eventually be required for commercial lithographic optics, making this a worst-

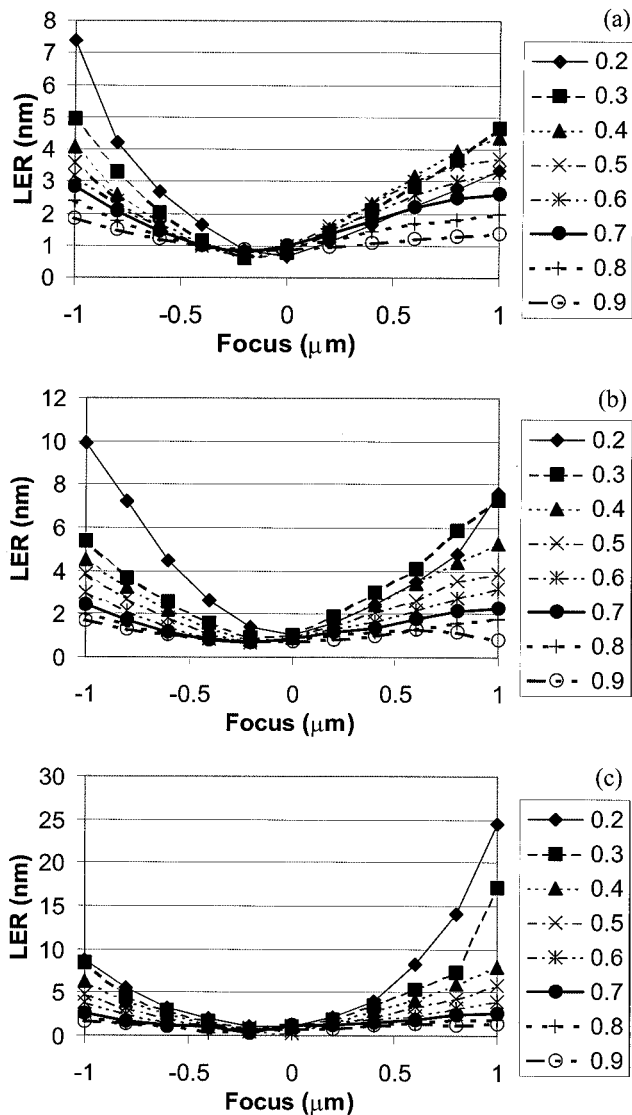


Fig. 6. LER modeling results, including the effects of projection optics aberrations. Aberrations based on the EUV engineering test stand (ETS) Set-2 optic with an rms wave-front error in the first 37 Zernikes of 0.69 nm. Each plot represents a different nested-feature size: (a) 100 nm, (b) 90 nm, and (c) 80 nm, with the individual traces representing different partial-coherence values.

case test. Figure 6 shows the LER results under these conditions. Other than the specific shapes of the plots (asymmetries induced by the aberrations), the results are similar to those obtained by assuming an ideal optic. A notable exception, however, is the aberrated-optic case, in which the LER-versus-partial-coherence trend no longer reverses at best focus. The faithful reproduction of the object-plane phase distribution is now limited by the aberrations in the optic.

4. Relevance of Mask Roughness to Print-Based Extreme-Ultraviolet Studies

Recent EUV exposure tests²⁸ performed with the ETS Set-2 optic in a variable- σ static exposure tool installed at the Lawrence Berkeley National Laboratory have

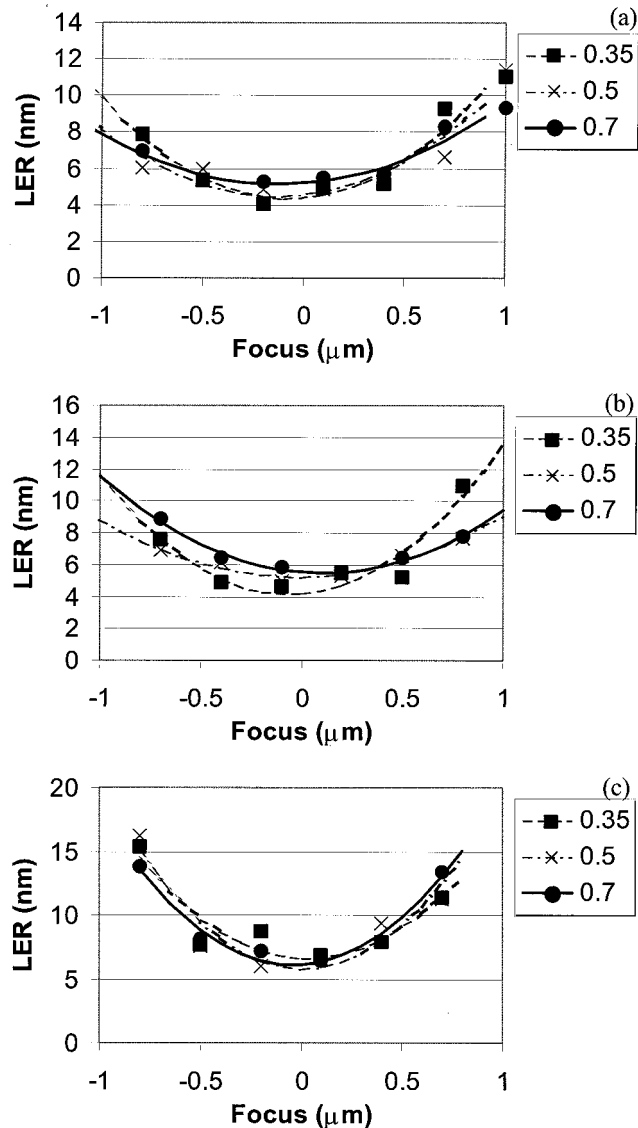


Fig. 7. Experimental LER results obtained from the ETS Set-2 optic operating in the Lawrence Berkeley static exposure tool. Each plot represents a different nested-feature size: (a) 100 nm, (b) 90 nm, and (c) 80 nm, with the individual traces representing different partial-coherence values. Symbols, the actual data; lines, quadratic fits to the data.

been used to characterize the performance (including LER) of the ETS projection optic and an EUV resist (EUV-2D, provided by Shipley Company). Here I consider the extent to which mask roughness may have contributed to observed LER limitations. Figure 7 shows experimental LER results through focus for various feature sizes and partial-coherence settings. Systematic trends in the data as a function of partial coherence are not observed, suggesting that mask roughness does not play a dominant role in the observed LER. To further quantify the predicted contribution from mask roughness, I make the assumption that mask-roughness-induced LER adds in quadrature to other contributors and calculate the predicted fractional contribution based on simulated LER

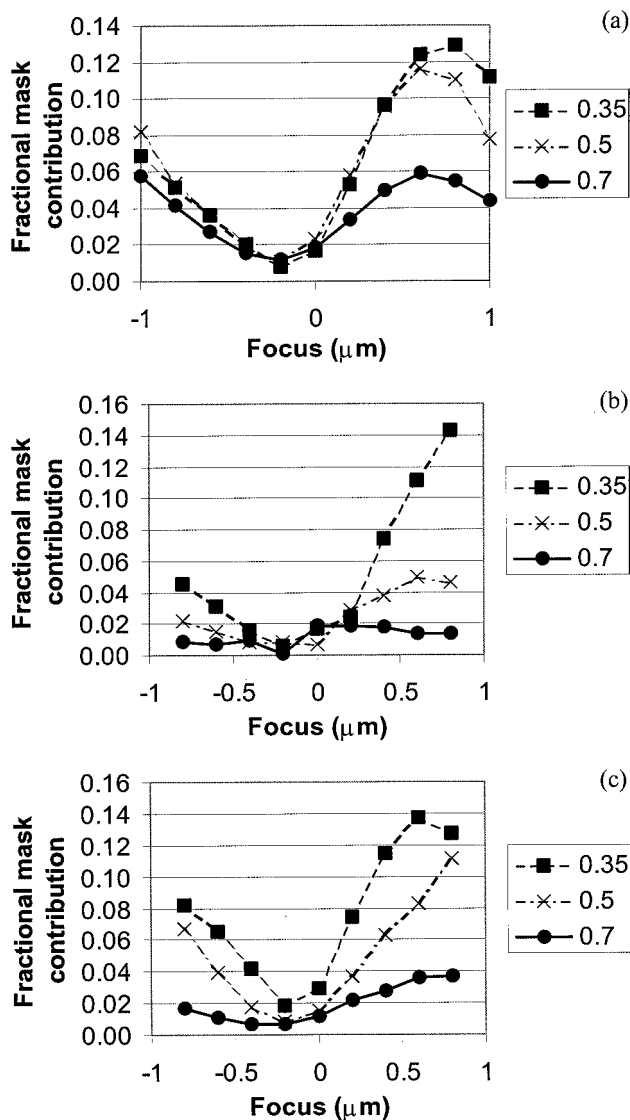


Fig. 8. Predicted fractional contribution of mask-roughness-induced LER to the experimentally observed LER from Fig. 7. Each plot represents a different nested-feature size: (a) 100 nm, (b) 90 nm, and (c) 80 nm, with the individual traces representing different partial-coherence values.

results as described above. Figure 8 shows the results that reveal a systematic increase in the mask-roughness fractional contribution as a function of defocus and increasing coherence, suggesting that mask roughness is responsible for an observable amount of LER in my experiments. In all cases the contribution is limited to less than 15%, and at best focus the contribution is negligible. Thus, even with 0.5-nm rms roughness, EUV masks can be used for meaningful LER screening of resists provided that focus is adequately controlled. I note that I have no explanation for the apparently anomalous behavior seen in the 100-nm line-space case.

The results presented above are based on an NA of 0.1; however, commercial EUV tools will be required to support NAs of 0.25 or larger. To make possible early

studies at relevant NAs, 5 \times reduction 0.3-NA microfield EUV optics (referred to as MET optics) are being developed.^{29,30} This two-mirror on-axis optical system has a central obscuration with a radius equal to 30% of the full 0.3 NA. Given the strong dependence of the imaging optic NA on mask roughness to LER coupling, it is important to repeat the above analysis at this higher NA in order to determine whether current mask technology is adequate for early LER-based screening of developmental EUV photoresists. To this end, I generate a new set of simulation masks that correspond to printed line widths ranging from 25 to 50 nm. To generate the roughness on the masks, I use the same PSD as described above while decreasing its magnitude by a factor of 2 to more accurately represent most recent mask-fabrication capabilities.³¹⁻³³ In all cases an annular illumination with an inner σ of 0.3 is assumed, whereas the outer σ is allowed to vary from 0.4 to 0.8. The simulated focus range is ± 150 nm, with ± 100 nm being the nominal design depth of focus for 30-nm features. The image-space pixel size used in the calculations is 0.78 nm.

Figure 9 shows the modeled LER results through focus for feature sizes from 50 to 40 nm; Fig. 10 those from 35 to 25 nm. The major trends are similar to those observed with the ETS optic in that the LER tends to worsen as the coherence is increased, the feature size is reduced, and the defocus is increased. The trend of improved LER with increased coherence at best focus is not evident in this case. This is most likely due to the fact that the inner annulus of the illumination is so close to the edge of the central obscuration, yielding significant filtering effects from the pupil. Other anomalies, such as decreasing LER with decreasing feature size at some coherence settings, are also observed. An example of this is the LER trend from 40 to 30 nm for outer σ of 0.5 and smaller. This is also expected to be caused by an interaction between the diffracted orders from the object pattern and the central obscuration. Finally, I note that these simulations show that at the edge of focus, the mask-roughness-induced LER accounts for the entire specified resist LER budget for the 45-nm node⁴ unless a very low coherence is used. This means that extreme care must be taken when such a system is used for LER screening of resist. The assumption that subsequent nodes have even tighter LER specifications renders the problem even more acute.

5. Summary

The problem of mask-reflection surface-roughness coupling to LER has been studied numerically for various practical cases. In general I find that the LER increases as coherence and defocus are increased. For the unobscured 0.1-NA optic I further observed the initially counterintuitive behavior of LER decreasing with increasing coherence at best focus. Comparing modeling results with actual exposures from a 0.1-NA EUV optic, I found present LER values to be nominally unaffected by mask roughness except at the edge of focus, where mask-

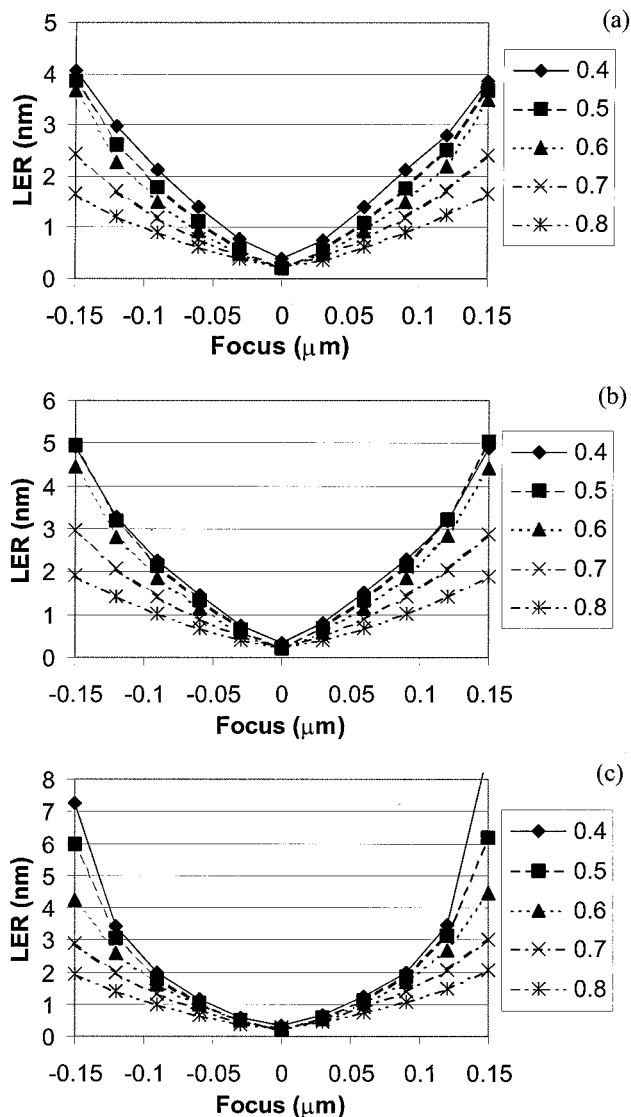


Fig. 9. LER modeling results for the 0.3-NA MET optic design. Each plot represents a different nested-feature size: (a) 50 nm, (b) 45 nm, and (c) 40 nm. In all cases the illumination is annular with an inner σ of 0.3, and the individual traces represent different outer σ values.

roughness contributions are limited to approximately 15%. Extending the analysis to the centrally obscured 0.3-NA MET optic, I found that, with current mask technology, care must be taken to maintain focus to better than 50 nm when the MET is used for LER-based resist screening. This is especially true in the case of low- σ illumination.

Although the modeling presented here specifically addresses the object-plane roughness problem for EUV lithography, it is evident that parallels can be drawn to many other short-wavelength applications such as microscopy or moiré interferometry. Moreover, the specific results presented here can be made essentially wavelength independent if one takes the object-plane phase-roughness value as described in radians to be constant.

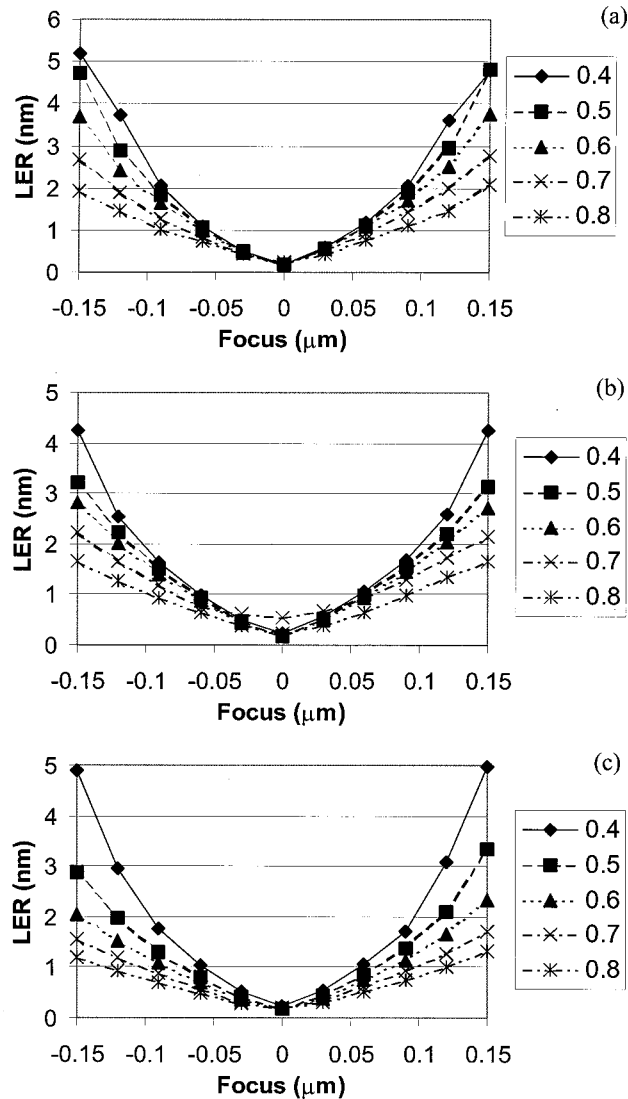


Fig. 10. LER modeling results for the 0.3-NA MET optic design. Each plot represents a different nested-feature size: (a) 35 nm, (b) 30 nm, and (c) 25 nm. In all cases the illumination is annular with an inner σ of 0.3, and the individual traces represent different outer σ values.

This research was performed at the Lawrence Berkeley National Laboratory and was supported by the Extreme Ultraviolet Limited Liability Company and by International Sematech. The Lawrence Berkeley National Laboratory is operated under the auspices of the Director, Office of Science, Office of Basic Energy Science, of the U.S. Department of Energy.

References and Notes

1. R. Stulen and D. Sweeney, "Extreme ultraviolet lithography," *IEEE J. Quantum Electron.* **35**, 694–699 (1999).
2. H. Meiling, J. Benschop, R. Hartman, P. Kürz, P. Høghøj, R. Geyl, and N. Harned, "EXSTATIC: ASML's α -tool development for EUVL," in *Emerging Lithographic Technologies VI*, R. L. Engelstad, ed., Proc. SPIE **4688**, 52–63 (2002).
3. K. Hamamoto, T. Watanabe, H. Hada, H. Komano, S. Kish-

- imura, S. Okazaki, and H. Kinoshita, "Fine pattern replication on 10×10 -mm exposure area using the ETS-1 laboratory tool in HIT," in *Emerging Lithographic Technologies VI*, R. L. Engelstad, ed., Proc. SPIE **4688**, 664–671 (2002).
4. International Technology Roadmap for Semiconductors, 2001 ed., <http://public.itrs.net/>.
 5. R. Brainard, C. Henderson, J. Cobb, V. Rao, J. Mackevich, U. Okoroanyanwu, S. Gunn, J. Chambers, and S. Connolly, "Comparison of the lithographic properties of positive resists upon exposure to deep- and extreme-ultraviolet radiation," *J. Vac. Sci. Technol. B* **17**, 3384–3389 (1999).
 6. M. Shumway, S. Lee, C. Cho, P. Naulleau, K. Goldberg, and J. Bokor, "Extremely fine-pitch printing with a $10\times$ Schwarzschild optic at extreme ultraviolet wavelengths," in *Emerging Lithographic Technologies V*, E. A. Dobisz, ed., Proc. SPIE **4343**, 357–362 (2001).
 7. W. Li, H. Solak, and F. Cerrina, "EUV nanolithography: sub-50 nm L/S," in *Emerging Lithographic Technologies IV*, E. A. Dobisz, ed., Proc. SPIE **3997**, 794–798 (2000).
 8. T. Watanabe, H. Kinoshita, A. Miyafuji, S. Irie, S. Shirayone, S. Mori, E. Yano, H. Hada, K. Ohmori, and H. Komano, "Lithographic performance and optimization of chemically amplified single-layer resists for EUV lithography," in *Emerging Lithographic Technologies IV*, E. A. Dobisz, ed., Proc. SPIE **3997**, 600–607 (2000).
 9. J. Goldsmith, K. Berger, D. Bozman, G. Cardinale, D. Folk, C. Henderson, D. O'Connell, A. Ray-Chaudhuri, K. Stewart, D. Tichenor, H. Chapman, R. Gaughan, R. Hudyma, C. Montcalm, E. Spiller, J. Taylor, J. Williams, K. Goldberg, E. Gullikson, P. Naulleau, and J. Cobb, "Sub-100-nm lithographic imaging with the EUV $10\times$ Microstepper," in *Emerging Lithographic Technologies III*, Y. Vladimirovsky, ed., Proc. SPIE **3676**, 264–271 (1999).
 10. P. Naulleau, K. Goldberg, E. Anderson, D. Attwood, P. Batson, J. Bokor, P. Denham, E. Gullikson, B. Harteneck, B. Hoef, K. Jackson, D. Olynick, S. Rekawa, F. Salmassi, K. Blaedel, H. Chapman, L. Hale, P. Mirkarimi, R. Souffi, E. Spiller, D. Sweeney, J. Taylor, C. Walton, D. O'Connell, R. Stulen, D. Tichenor, C. Gwyn, P. Yan, and G. Zhang, "Sub-70-nm EUV lithography at the Advanced Light Source Static Microfield Exposure Station using the ETS Set-2 Optic," *J. Vac. Sci. Technol. B* **20**, 2829–2833 (2002).
 11. P. Naulleau and G. Gallatin, "The line-edge roughness transfer function and its application to determining mask effects in EUV resist characterization," *Appl. Opt.* **42**, 3390–3397 (2003).
 12. N. Beaudry and T. Milster, "Effects of object roughness on partially coherent image formation," *Opt. Lett.* **25**, 454–456 (2000).
 13. N. Beaudry and T. Milster, "Effects of mask roughness and condenser scattering in EUVL systems," in *Emerging Lithographic Technologies III*, Y. Vladimirovsky, ed., Proc. SPIE **3676**, 653–662 (1999).
 14. J. W. Goodman, *Statistical Optics* (Wiley, New York, 1985), Chap. 7, pp. 286–360.
 15. PROLITH is a registered trademark of KLA-Tencor Corporation, 160 Rio Robles, San Jose, Calif. 95134.
 16. SOLID-C is a registered trademark of SIGMA-C GmbH, Thomas-Dehler-Str. 9, 81737 München, Germany.
 17. J. H. Underwood and T. W. Barbee, Jr., "Layered synthetic microstructures as Bragg diffractors for X rays and extreme ultraviolet: theory and predicted performance," *Appl. Opt.* **20**, 3027–3034 (1981).
 18. D. Stearns, "Stochastic model for thin film growth and erosion," *Appl. Phys. Lett.* **62**, 1745–1747 (1993).
 19. D. Stearns and E. Gullikson, "Nonspecular scattering from extreme ultraviolet multilayer coatings," *Physica B* **283**, 84–91 (2000).
 20. Z. Zhongrong, K. Lucas, J. Cobb, S. Hector, and A. Strojwas, "Rigorous EUV mask simulator using 2D and 3D waveguide methods," in *Emerging Lithographic Technologies VII*, R. L. Engelstad, ed., Proc. SPIE **5037**, 494–503 (2003).
 21. A. Erdmann, C. Kalus, T. Schmoller, and A. Wolter, "Efficient simulation of light diffraction from three-dimensional EUV masks using field decomposition techniques," in *Emerging Lithographic Technologies VII*, R. L. Engelstad, ed., Proc. SPIE **5037**, 482–493 (2003).
 22. T. Pistor, T. Y. Deng, and A. Neureuther, "Extreme ultraviolet mask defect simulation: Low-profile defects," *J. Vac. Sci. Technol. B* **18**, 2926–2929 (2000).
 23. E. Gullikson, C. Cerjan, D. Stearns, P. Mirkarimi, and D. Sweeney, "Practical approach for modeling extreme ultraviolet lithography mask defects," *J. Vac. Sci. Technol. B* **20**, 81–86 (2002).
 24. K. Goldberg, P. Naulleau, J. Bokor, and H. Chapman, "Testing EUV optics with visible-light and EUV interferometry," *J. Vac. Sci. Technol. B* **20**, 2834–2839 (2002).
 25. D. Tichenor, W. Replogle, S. Lee, W. Ballard, G. Kubiak, L. Klebanoff, J. Goldsmith, J. Wronosky, L. Hale, H. Chapman, J. Taylor, K. Goldberg, and P. Naulleau, "Performance upgrades in the EUV engineering test stand," in *Emerging Lithographic Technologies VI*, R. L. Engelstad, ed., Proc. SPIE **4688**, 72–86 (2002).
 26. D. O'Connell, S. Lee, D. Tichenor, W. Ballard, L. Bernardez, J. Goldsmith, S. Haney, K. Jefferson, T. Johnson, A. Leung, W. Replogle, J. Bjorkholm, E. Panning, P. Naulleau, H. Chapman, S. Wurm, G. Kubiak, and C. Gwyn, "Lithographic characterization of improved projection optics in the EUVL engineering test stand," in *Emerging Lithographic Technologies VII*, R. L. Engelstad, ed., Proc. SPIE **5037**, 83–94 (2003).
 27. D. W. Sweeney, R. Hudyma, H. N. Chapman, and D. Shafer, "EUV optical design for a 100-nm CD imaging system," in *Emerging Lithographic Technologies II*, Y. Vladimirovsky, ed., Proc. SPIE **3331**, 2–10 (1998).
 28. P. Naulleau, K. Goldberg, E. Anderson, J. Bokor, B. Harteneck, K. Jackson, D. Olynick, F. Salmassi, S. Baker, P. Mirkarimi, E. Spiller, C. Walton, D. O'Connell, P. Yan, and G. Zhang, "Printing-based performance analysis of the ETS Set-2 optic using a synchrotron exposure station with variable sigma," *J. Vac. Sci. Technol. B* **21**, 2697–2700 (2003).
 29. J. Taylor, D. Sweeney, R. Hudyma, L. Hale, T. Decker, G. Kubiak, W. Sweatt, and N. Wester, "EUV Microexposure Tool (MET) for near-term development using a high NA projection system," *Proceedings of the 2nd International EUVL Workshop* (International Sematech, Austin, Tex., 2000).
 30. R. Hudyma, J. Taylor, D. Sweeney, L. Hale, W. Sweatt, and N. Wester, "E-D characteristics and aberration sensitivity of the Microexposure Tool (MET)," *Proceedings of the 2nd International EUVL Workshop* (International Sematech, Austin, Tex., 2000).
 31. S. Hector, "EUVL masks: requirements and potential solutions," in *Emerging Lithographic Technologies VI*, R. L. Engelstad, ed., Proc. SPIE **4688**, 134–149 (2002).
 32. P. Mirkarimi, E. Spiller, D. Stearns, V. Sperry, and S. Baker, "An ion-assisted Mo-Si deposition process for planarizing reticle substrates for extreme ultraviolet lithography," *IEEE J. Quantum Electron.* **37**, 1514–1516 (2001).
 33. T. Ogawa, M. Ito, H. Yamanashi, H. Hoko, E. Hoshino, and S. Okazaki, "Simulation studies of roughness-smoothing effect of molybdenum/silicon multilayer coating based on resputtering model," in *Emerging Lithographic Technologies VI*, R. L. Engelstad, ed., Proc. SPIE **4688**, 716–724 (2002).